Biophysical*Journal*
Article

Biophysical Society

Cooperative Function of LL-37 and HNP1 Protects Mammalian Cell Membranes from Lysis

Ewa Drab[2] and Kaori Sugihara[1,2,*]
[1]Institute of Industrial Science, The University of Tokyo, Tokyo, Japan and [2]Department of Physical Chemistry, University of Geneva, Geneva, Switzerland

ABSTRACT LL-37, cleaved from human cathelicidin, and human neutrophil peptide-1 (HNP1) from the defensin family are antimicrobial peptides that are occasionally co-released from neutrophils, which synergistically kill bacteria. We report that this couple presents another type of cooperativity against host eukaryotic cells, in which they antagonistically minimize cytotoxicity by protecting membranes from lysis. Our results describe the potential of the LL-37/HNP1 cooperativity that switches from membrane-destructive to membrane-protective functions, depending on whether the target is an enemy or a host.

SIGNIFICANCE A mixture of different types of biomolecules sometimes boosts or suppresses their activities or even generates a new function known as cooperativity. We report a unique cooperative function between two well-known antimicrobial peptides (LL-37/HNP1) that kills bacteria more efficiently while minimizing the host damage by suppressing mammalian cell membrane lysis. Such a "double cooperativity" may be used in our immune system and may help with developing efficient and safe antimicrobial agents in the future.

INTRODUCTION

Synergy among antimicrobial peptides (AMPs) (1–19), in which mixing different types of AMPs boosts their antimicrobial efficiency, has garnered attention as a possible approach to improve their potency and because of its underlying interesting mechanism (2,20–25). Particularly, synergy between the cathelicidin-derived peptide (26), LL-37, and human neutrophil peptide 1 (HNP1) from the α-defensin subfamily (27–30) is important because they are among major human AMPs. LL-37 and HNP1 are mainly produced in the bone marrow during neutrophil maturation, which are then occasionally co-released into the blood and tissues for synergistically combating pathogens (10). However, LL-37 is known to exhibit cytotoxicity at high concentrations because of its membrane-destructive properties (31). How the host eukaryotic cells escape from their attack is unknown.

In this work, to study the effect of their cooperativity on host cells, mammalian cells and mammalian cell membrane mimics were challenged by LL-37, HNP1, and their mixture, and their responses were observed by biophysical assays based on supported and pore-spanning bilayers, such as fluorescence recovery after photobleaching (FRAP), quartz crystal microbalance with dissipation (QCM-D), electrochemical impedance spectroscopy (EIS), and single-channel conductance measurement, which we have routinely employed for membrane-active compound characterization for the past years (32–38), combined with toxicity test by calcium-sensitive dye, several spectroscopic methods, and electron-beam microscopy. The result showed that this couple cooperatively protects mammalian cell membranes from lysis for minimizing the cytotoxicity in contrast to known synergistic effect against bacteria.

MATERIALS AND METHODS

For a detailed summary of the materials and methods used in this study, see Supporting Material.

RESULTS

HNP1 unexpectedly suppresses LL-37 cytotoxicity in MDCK cells and HUVEC

Apart from its antimicrobial activities (39), LL-37 is a well-known key player of several biological processes in the host, such as immunomodulation (40), the promotion of cell

---

Submitted August 26, 2020, and accepted for publication October 8, 2020.

*Correspondence: kaori-s@iis.u-tokyo.ac.jp

Editor: Charles Deber.

https://doi.org/10.1016/j.bpj.2020.10.031

motility, and wound healing (39–42), whereas it becomes cytotoxic at high concentrations (>2.5–13 μM (40,43,44)). This cytotoxicity of LL-37 toward mammalian cells could be visualized by calcium-sensitive dyes in a time-dependent manner. The addition of LL-37 to Madin-Darby canine kidney (MDCK) cells at 29 μM resulted in a fluorescence increase from the intracellular calcium reporter, Fluo-3, within 3 min (Fig. 1 *a*, *first row*), indicating its cytotoxicity. The rapid response time implies defect formation in the plasma membrane and the subsequent induction of a large calcium influx from the extracellular space into the cytosol, as has been reported previously (45). This pore-induced cytotoxicity was inhibited by the mixture of LL-37 and HNP1 at a 1:1 molar ratio (Fig. 1 *a*, *third row*). The control experiment showed that HNP1 individually did not induce noticeable cytotoxicity at 29 μM (Fig. 1 *a*, *second row*). The similar HNP1-related inhibition of LL-37 cytotoxicity was observed in human umbilical vein endothelial cells (HUVEC), as shown in Fig. 1 *b*. Note that the timescale required to induce the LL-37 cytotoxicity in HUVEC was 50 times longer; thus, this might have involved other mechanisms than a simple pore formation. These results show that HNP1 neutralizes LL-37 cytotoxicity in MDCK cells and HUVEC in contrast to the previously reported synergy against bacteria (10).

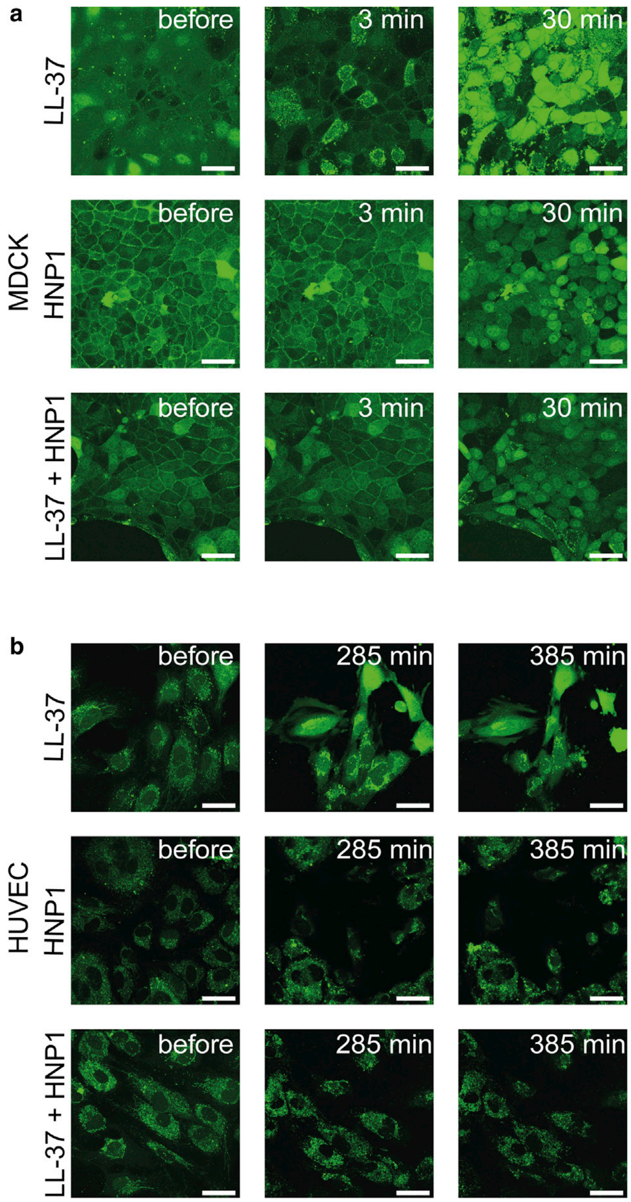

FIGURE 1 Cytotoxic activity of LL-37 and its inhibition by HNP1, studied with calcium sensitive dye, Fluo-3. (*a*) MDCK and (*b*) HUVEC with Fluo-3 are monitored by confocal laser scanning microscopy over time, where after 350 s for MDCK and 1292 s for HUVEC, LL-37, HNP1, and their mixture at 1:1 molar ratio were added all at 29 μM (in the case of the mixture, it is 29 μM LL-37 + 29 μM HNP1). Scale bars, 10 μm. To see this figure in color, go online.

LL-37 and HNP1 did not interact in solution

To study whether LL-37 and HNP1 already bind in solution, their interactions in a physiological HEPES buffer solution (150 mM NaCl (pH 7.4)) were monitored using isothermal titration calorimetry (ITC), tryptophan fluorescence spectroscopy, and circular dichroism (CD). No clear evidence for their binding was observed in ITC, as seen by the constant endothermal peaks that come from heats of dilution during the titration of LL-37 into HNP1 in a HEPES buffer solution (Fig. 2 *a*). To confirm this result, we measured the HNP1 tryptophan fluorescence emission peak both in the presence and absence of LL-37. HNP1 has a single tryptophan (Trp) residue, which causes a blue shift in its emission peak in a hydrophobic microenvironment. We observed no change in the tryptophan emission peak position between with or without LL-37 (Fig. 2 *b*), indicating no interaction. This was further validated by CD, in which the double-dip at 208 and 222 nm characteristic for α-helical structures (46) in LL-37 remained unchanged after the addition of HNP1 (Fig. 2 *c*), suggesting the absence of structural rearrangements often observed upon binding (17).

ITC results show no significant effect of HNP1 on the LL-37 adsorption onto the POPC bilayers

Because bilayer disruption is one of the well-known mechanisms of LL-37 toxicity, its suppression by HNP1 might be taking place in the membranes. As a first step toward better understanding such a cooperative function in membranes, we studied their adsorption to 1-palmitoyl-2-oleoyl-glycero-3-phosphocholine (POPC), which is one of the major lipids in eukaryotic plasma membranes. We titrated peptides with POPC vesicles in ITC. LL-37 bound to POPC vesicles (Fig. 3 *a*). The binding is strongly entropic ($-T\Delta S = -6.258$ kcal/mol $<< \Delta H = -0.194$ kcal/mol, where $\Delta G = \Delta H - T\Delta S = -6.452$ kcal/mol), indicating that the hydrophobic interaction was the main cause of the binding rather than the electrostatic interaction. Note that these values are rough

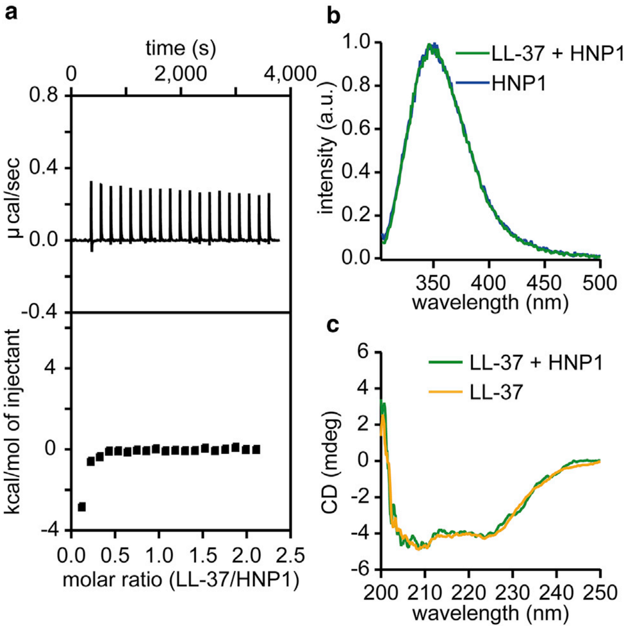

FIGURE 2 LL-37 and HNP1 did not interact in solution, evidenced by isothermal titration calorimetry (ITC), tryptophan (Trp) fluorescence spectroscopy, and CD. (*a*) Heat flow and the integrated heat from ITC when 40 μM HNP1 in HEPES buffer solution in a chamber volume of 200 μL was titrated with 400 μM LL-37 in HEPES buffer solution at 2 μL each time for 20 times. (*b*) Shown are Trp fluorescence emission spectra of HNP1 alone in HEPES buffer solution at 2.9 μM and in combination with LL-37 at 1:1 molar ratio (LL-37 signal subtracted). (*c*) Shown are CD spectra of LL-37 in HEPES buffer solution at 29 μM and in combination with HNP1 at 1:1 molar ratio (HNP1 signal subtracted). All measurements were done in 10 mM HEPES and 150 mM NaCl at pH 7.4. To see this figure in color, go online.

estimations as the ITC signals also contain the information on peptide arrangements in the bilayers, such as pore formation, in addition to binding (47,48). Titration of vesicles to HNP1 did not produce any detectable amount of heat from binding as no titration curve was observed (Fig. 3 *a*). Fluorescence microscopy and quartz crystal microbalance with dissipation monitoring confirmed the adhesion of HNP1 to POPC bilayers, as we will discuss later (Fig. 3, *c* and *e*). Thus, this lack of significant heat production upon binding is the result of a too entropic interaction, which was below the ITC sensitivity at this concentration. The mixture of LL-37 and HNP1 yielded a titration curve similar to that of LL-37 (Fig. 3 *a*). This suggests that the LL-37 adhesion to POPC vesicles was affected little by the presence of HNP1. The vesicle sizes, estimated by dynamic light scattering, were not altered significantly by the addition of peptides (Fig. 3 *b*).

FRAP results demonstrate LL-37-induced POPC bilayer destruction, rescued by the addition of HNP1

The first evidence for the interference of LL-37 and HNP1 was observed during FRAP, as shown in Fig. 3 *c*. FRAP is a well-established tool for the characterization of the lipid bilayer integrity and fluidity (49). Supported POPC + 0.2% mol 1,2-dioleoyl-*sn*-glycero-3-phosphoethanolamine-N-(7-nitro-2-1,3-benzoxadiazol-4-yl lipid bilayers were assembled on glass coverslips by vesicle fusion as confirmed by full FRAP recovery with a diffusion coefficient of $D = 3.38 \pm 0.25\ \mu m^2/s$ (Fig. 3 *d*). These results were comparable with previously published values (49). LL-37 disrupted the lateral continuity of these bilayers at 2.9 μM, as demonstrated by a lack of FRAP recovery (Fig. 3, *c* and *d*). The decreased fluorescence intensity from the bilayer indicated the detachment of lipids from the substrate upon the addition of LL-37 (Fig. 3 *c*). HNP1 induced membrane protrusions, demonstrated by the appearance of bright dots in the fluorescence images (Fig. 3 *c*). Nevertheless, the bilayer maintained the lateral continuity as FRAP showed a full recovery with a diffusion coefficient of $D = 2.14 \pm 0.48\ \mu m^2/s$, which was 37% reduced compared to the POPC bilayers without peptides. This illustrates that HNP1 inserted into the bilayers and increased the surface area of the membranes, where the excess area folded into structures such as tubes are visible as bright spots, without disintegrating the bilayer. The mixture of LL-37 and HNP1 interacted with the bilayer as some bright dots were also observed after the incubation, yet the bilayer continuity was maintained, confirmed by the full FRAP recovery with a reduced diffusion coefficient of $D = 2.14 \pm 0.81\ \mu m^2/s$ (Fig. 3, *c* and *d*). These FRAP data provided evidence to the LL-37-induced POPC bilayer destruction, whereas adding HNP1 rescued this effect. Such a cooperative function between LL-37 and HNP1 in synthetic POPC bilayers might be linked to the observed neutralization of cytotoxicity shown in Fig. 1.

QCM-D indicates that LL-37 removes lipids from bilayers, HNP1 creates membrane protrusions, and their mixture suppresses both effects

To confirm the observed peptide-bilayer interactions, we next used QCM-D. QCM-D enables the detection of wet mass (including the water mass) on the sensor crystal and the viscoelastic properties of the deposited film by the changes in the resonance frequency Δf and the decay of the sensor oscillations ΔD (50), frequently used to study AMP-bilayer interactions (51). Supported POPC bilayers were formed on silicon dioxide-coated quartz crystal microbalance crystals by vesicle rupture, as confirmed by the typical frequency and dissipation change in QCM-D during this process. The initial decrease in Δf (increase in mass) and the increase in ΔD indicated the vesicle adsorption, whereas the following increase (decrease in mass) and the stabilization of Δf at around 24 Hz and the decrease in ΔD illustrated the vesicle rupture and the corresponding release of water mass (Fig. 3 *e*, bilayer formation; (52)). LL-37 partially removed lipids from the

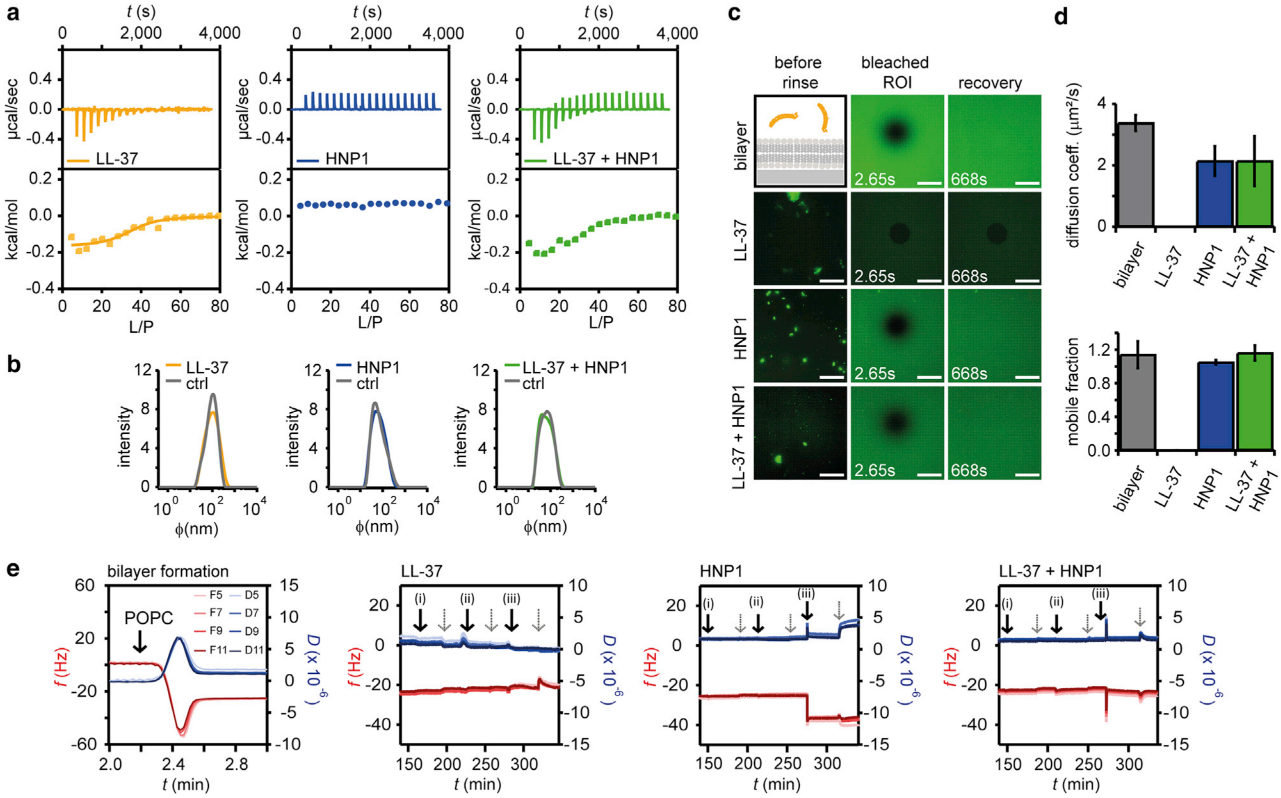

FIGURE 3 Peptide-lipid interactions monitored by ITC, fluorescence recovery after photobleaching (FRAP), and QCM-D. (*a*) Heat flow and the integrated heat from ITC when LL-37, HNP1, and LL-37 + HNP1 at 1:1 molar ratio all at 40 μM (in case of the mixture 40 μM each) in the chamber volume of 200 μL were titrated with POPC vesicles at 15 mM with 2 μL each time for 20 times. The reverse titration is shown in Fig. S1. (*b*) Vesicle size after each ITC experiment was determined by dynamic light scattering. (*c*) Shown are fluorescence images of supported POPC lipid bilayers with 0.2% mol 1,2-dioleoyl-*sn*-glycero-3-phosphoethanolamine-N-(7-nitro-2-1,3-benzoxadiazol-4-yl after incubation with each peptide at 2.9 μM before rinsing and subsequent FRAP images after rinsing. Note that the enhancement is different between before and after the rinse to visualize the bright dots in the images before rinse. Scale bars, 50 μm. (*d*) Diffusion coefficients were calculated from FRAP experiments as follows: 3.38 ± 0.25 $\mu m^2/s$ for the POPC bilayers, no recovery was observed for LL-37, 2.14 ± 0.48 $\mu m^2/s$ for HNP1, and 2.14 ± 0.81 $\mu m^2/s$ for the peptide mixture. Experiments were repeated for three times and their average and the standard deviation are plotted. (*e*) Shown are QCM-D data for the bilayer formation by vesicle rupture and the subsequent addition of LL-37, HNP1, and their mixture at (i) 0.29 μM, (ii) 2.9 μM, and (iii) 29 μM. The gray dotted arrows indicate the rinse by injecting HEPES buffer solution. Their overtone analysis is shown in Fig. S2. To see this figure in color, go online.

sensor surface and made the bilayer slightly more rigid, implied by the increase in frequency (a loss in mass) and the decrease in dissipation (Fig. 3 *e*). The mass of LL-37 is too small to be detected because even a monolayer membrane coverage would have resulted only in $\Delta f = 2–4$ Hz (53,54). Further overtone analysis provided a resolution in a *z*-direction as acoustic wave penetration depths decrease along with the increasing overtone numbers (55,56). No significant overtone dependency except for a slight variation in Δf at the highest concentration (29 μM, Fig. S2, *a* and *b*) was observed, in agreement with the previously reported detergent-like mechanism (57). HNP1 induced a reduction in Δf by 13.6 Hz (increase in mass) and increase in dissipation by 2.4×10^{-6} after the last rinse (Fig. 3 *e*), indicating the lipid bilayer morphological change and the associated increase in the coupling of water mass typical for the membrane protrusion or vesicle adsorption (52). This is in agreement with the appearance of bright dots in fluorescence images (Fig. 3 *c*). A slight overtone dependence (Fig. S2, *c* and *d*), visible at 29 μM, both in Δf and ΔD also suggests that the main mass increase took place at least tens of nanometers away from the sensor surface (58), which is compatible with the membrane protrusion. The mixture of LL-37 and HNP1 showed no significant signal change (Fig. 3 *e*; Fig. S2, *e* and *f*), indicating that the effect of LL-37 (destruction) and HNP1 (protrusion) on supported bilayers are both suppressed when they are mixed.

EIS confirms that HNP1 suppresses LL-37 defect formation

Next, to monitor the bilayer destruction process with higher sensitivity, we performed EIS. We used supported POPC lipid bilayers formed on highly doped (metallic) silicon wafers as a working electrode in a three-electrode setup. The

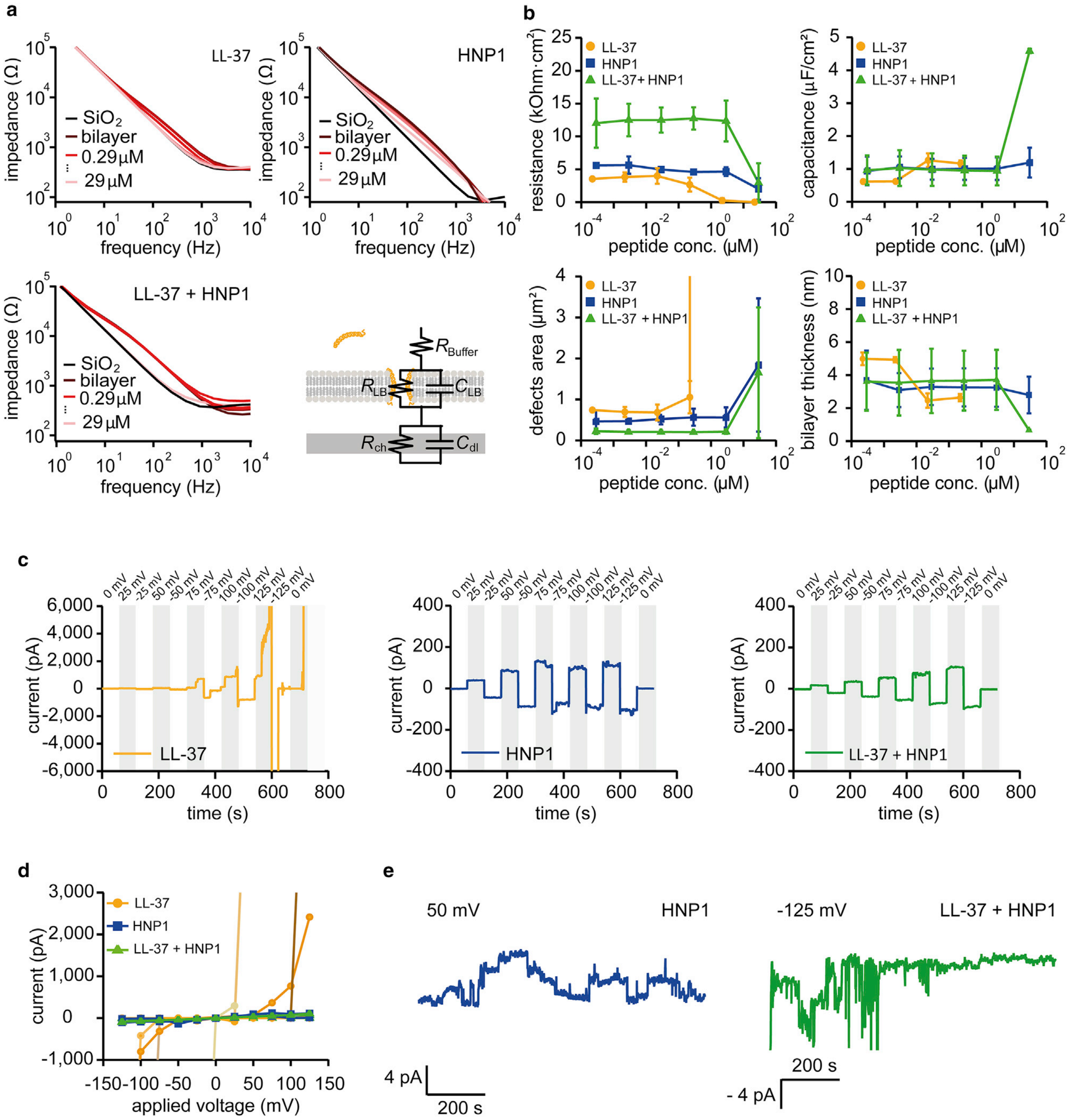

FIGURE 4 EIS with supported lipid bilayers and conductance measurements with porespanning bilayers confirm that HNP1 suppresses LL-37 membrane disintegration. (*a*) Shown are EIS spectra of supported POPC bilayers at different peptide concentrations. An equivalent circuit used for fitting is also shown. (*b*) Extracted bilayer resistance and capacitance and their conversion into defect area and bilayer thickness were plotted against peptide concentrations. Experiments were repeated twice and their average and the standard deviation are plotted. (*c*) Shown are current recordings through free standing lipid bilayer with the addition of LL-37 at 8 μM, HNP1 at 8 μM, and LL-37+HNP1 at 1:1 molar ratio with the total peptide concentration of 16 μM at different applied voltages and (*d*) extracted *I-V* plot. For each peptide, multiple runs were analyzed and presented in the *I-V* plot. (*e*) Shown are conductance measurements of pore-spanning lipid bilayers exposed to HNP1 at 15 μM at 50 mV holding potential and LL-37+HNP1 mixture at 1:1 molar ratio with the total concentration of 26 μM at -125 mV holding potential. To see this figure in color, go online.

top surface of silicon is silicon dioxide, which facilitates the self-assembly of bilayers by vesicle fusion. From the obtained impedance spectra (Fig. 4 *a*), a bilayer resistance R_{LB} and a capacitance C_{LB} were extracted (Fig. 4 *b*) by fitting them with an equivalent circuit presented in Fig. 4 *a*. Both R_{LB} and C_{LB} were further converted into the total defect area and the average bilayer thickness. LL-37 destroyed bilayers at 2.2 μM, indicated by an abrupt increase in the defect area (Fig. 4 *b*, defect area). LL-37 is known to form defects in a concentration-dependent manner, both in bacterial and eukaryotic cell membrane mimics, previously shown by vesicle leakage assay (59). In contrast, HNP1 created a total defect size of 1.6 μm^2 at 29 μM (Fig. 4 *b*, defect area), suggesting that HNP1 also forms small defects at such a high concentration. When they were mixed, the total defect area became 0.3 μm^2 at 29 μM, indicating that HNP1 suppressed the LL-37-induced bilayer destruction. The average bilayer thickness started to decrease at the LL-37 concentration of 0.22 μM (Fig. 4 *b*, bilayer thickness). Beyond 2.2 μM, the thickness could not be estimated because the bilayer was destroyed. For HNP1 and the mixture, the average bilayer hydrocarbon thickness was 3.2 and 3.1 nm, both at 2.9 μM. These impedance data further confirm that LL-37 forms large defects in bilayers, whereas the mixture of HNP1 rescues it.

Single-channel conductance indicates that LL-37 alters the behavior of the HNP1 pores

Next, the bilayer conductance was measured at a fixed (DC) voltage with lateral pore-spanning bilayers as described previously (36,38). After a giga-Ohm seal was achieved, LL-37, HNP1, and their mixture were added to the *cis* chamber, and step voltages from 0 to 125 mV/−125 mV were applied. For LL-37, transmembrane currents exceeded 6000 pA at ±125 mV (Fig. 4 *c*), or the bilayer often ruptured. These dramatic effects on the bilayers were in agreement with the previously proposed carpet-like mechanism for LL-37-bilayer interaction (60). For HNP1 and its mixture with LL-37, the transmembrane currents never exceeded 200 pA at ±125 mV (Fig. 4 *c*). These results further confirm that LL-37 forms large defects in bilayers, whereas the addition of HNP1 suppresses it. In between these conductance measurements, we ran impedance spectroscopy to monitor the change in the bilayer thickness. The standard POPC bilayers have a capacitance density of 0.6–1.0 $\mu F/cm^2$ (61–63), which corresponds to the thickness of around 4 nm. In the case of LL-37, defects in bilayers were observed even at a capacitance as low as 0.3 $\mu F/cm^2$ (Fig. S3), which corresponds to the bilayer thickness of 10.4 nm because of the remaining organic solvent sandwiched between the two monolayer leaflets. This indicated that LL-37 formed defects independent of the bilayer thickness as in the carpet-like model (60). Bilayer conductance measurement at a fixed voltage captured single channels for HNP1. The size of these pores was around 1.2 ± 0.2 Å at −50 mV (Fig. 4 *e*), although the pore size seemed to fluctuate as other channel conductance were also seen. This single pore conductance appeared to be disturbed when LL-37 was mixed (Fig. 4 *e*). These results suggest that LL-37 destabilizes bilayers, HNP1 forms small stable pores at high concentrations (15 μM), and their mixture forms small defects without rupturing bilayers.

Cryo-electron microscopy visualized that LL-37 destroys POPC vesicles into small fragments, HNP1 creates a stable opening in vesicles, and their mixture forms bilayer sheets or nanodisks

To visualize the peptide-induced lipid structural change, POPC vesicles incubated with LL-37, HNP1, and their mixture were imaged by cryo-transmission electron microscopy (cryo-TEM). LL-37 disintegrated lipid membranes, captured by small fragments of lipid-peptide composites (Fig. 5 *a*) with a size ranging from 4.8 to 19.4 nm (the average was 9.7 ± 2.8 nm) that did not exist before adding LL-37 (a control image shown in Fig. S4). These fragments were not observed with POPC vesicles incubated with HNP1 (Fig. 5 *b*). Instead, a stable perforation of bilayers by HNP1, which created openings in vesicles, was observed (*arrows* in Fig. 5 *b*). The mixture of LL-37 and HNP1 produced objects that resembled nanodisks and sheets (Fig. 5 *c*). Recently, several amphiphilic proteins have been shown to spontaneously assemble into lipid-protein nanodisks, in which these proteins wrap lipid bilayer disks like a belt to reduce the line tension at the bilayer edge (64–66). Although we acquired these images at rather high concentrations (lipid concentration = 1.5 mM, peptide concentration = 150 μM, L/P = 10) to adjust the density of the objects compatible with cryo-TEM, the LL-37-induced bilayer destruction and its partial inhibition by HNP1 is in agreement with our other data.

DISCUSSION

LL-37 is a 37 residue, amphipathic, human helical peptide, expressed in epithelial cells of the testis, skin, gastrointestinal tract, and respiratory tract, as well as in leukocytes, such as monocytes, neutrophils, T cells, natural killer cells, and B cells. It has been found to have antimicrobial (10), antiviral (67), and anticancer (68) activities, as well as immunomodulatory roles comprising both anti- (69) and proinflammatory functions (70), chemotactic (71), and cytotoxic effect (44), and it also promotes cell migration and wound closure (72). HNP1 is a 30-amino acid human peptide adopting a triple-stranded β-sheet structure (73). It is released from cells upon stimuli or, in some cases, constitutively, for example from neutrophils, natural killer cells, and monocytes, and exhibits antimicrobial activity (74,75), neutralizes bacterial toxins (76), and modulates the adaptive immune response (77). Bilayer membranes are the primary targets of LL-37 and HNP1; thus, these peptides affect fungi (78,79) and enveloped viruses (67,80) besides bacteria. LL-37 and HNP1 are frequently co-expressed. In 2000, Nagaoka and co-workers reported direct evidence of their synergistic antimicrobial effect against *Escherichia coli* and *Staphylococcus aureus* (10). In this study, we observed the opposite, an antagonistic effect toward MDCK cells and HUVEC, in which the LL-37 cytotoxicity is suppressed by HNP1 (Fig. 1). The previous report, in addition to our result,

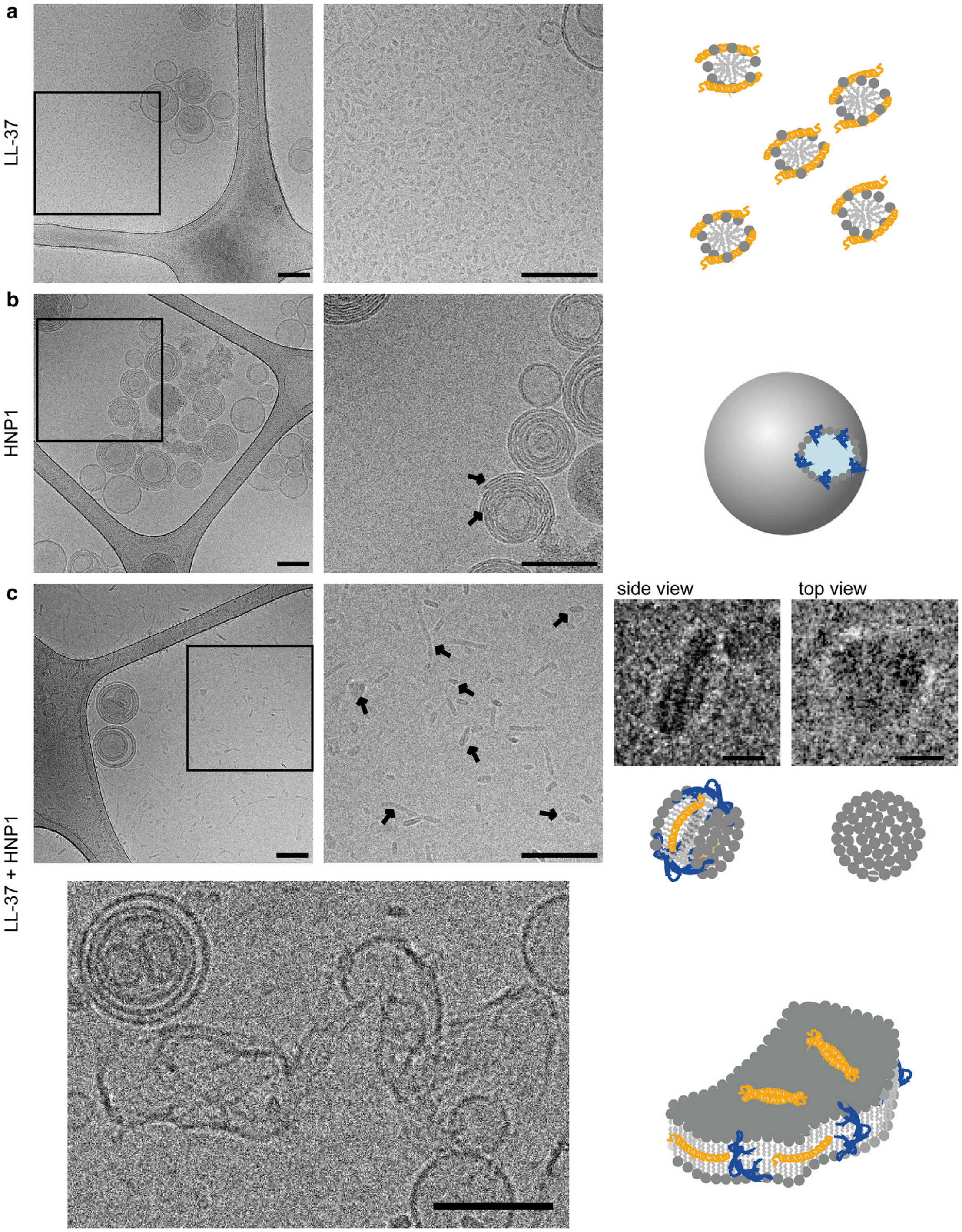

FIGURE 5 Cryo-electron microscopy visualized that LL-37 destroys POPC vesicles into small fragments, HNP1 creates stable opening in vesicles, and their mixture forms bilayer sheets or nanodisks. Shown are cryo-electron microscopy (cryo-TEM) images of POPC vesicles after incubation with (*a*) LL-37, (*b*) HNP1, and (*c*) LL-37 + HNP1 mixture. Peptides at 150 μM were incubated with vesicles at 1.5 mM for 30 min in physiological HEPES buffer solution. In the case of the mixture, 300 μM was the final concentration of both peptides combined (150 μM LL-37 + 150 μM HNP1). Possible interpretation of these images is drawn on the right side. All images were taken with Talos TEM 200 kV, except the one at the bottom, which was taken by Titan Krios G3i 300 kV. All the scale bars represents 100 nm except for the zoom-in top and side-view images of nanodisks, which are 10 nm. To see this figure in color, go online.

implies that the cooperative function of the LL-37/HNP1 pair might switch from destructive to protective, depending on the target. Our data showed that LL-37 and HNP1 did not bind in solution, as confirmed by ITC, tryptophan fluorescence spectroscopy, and CD (Fig. 2). Previously LL-37 has been reported to form dimers, trimers, or tetramers

(81–83) in solution, whereas HNP1 has been shown to form dimers (84). Their oligomerization in aqueous solution is driven by the minimization of their free energy to hide their hydrophobic residues from the surrounding water. Once their hydrophobic parts have been already concealed as oligomers, their net positive charge would induce an electrostatic repulsion between LL-37 and HNP1. This partially explains the lack of their binding in solution. LL-37 adhesion to POPC bilayers was not significantly affected by the presence of HNP1 either, indicated by ITC (Fig. 3 *a*). We found evidence for their interaction only after they bound to bilayers. LL-37 formed large defects or destroyed bilayers that were visible in FRAP (Fig. 3, *c* and *d*), QCM-D (Fig. 3 *e*), EIS (Fig. 4, *a* and *b*), transmembrane currents (Fig. 4, *c* and *d*), and cryo-TEM (Fig. 5 *a*). The mechanism of the LL-37 interaction with membranes is still debated. However, several models have been proposed, depending on the applied method. Carpet/toroidal membrane disintegration has been proposed based on solid-state NMR studies for LL-37 interacting with different membranes (85). The parallel orientation of peptide to membrane surface was confirmed by attenuated total reflection Fourier-transform infrared spectroscopy (ATR-FTIR) (82), supporting a carpet-like mechanism. Some studies suggest that LL-37 could distinguish anionic and zwitterionic lipids (86). However, other studies have shown a lack of such discrimination (82). HNP1 induces protrusions in bilayers, as we observed by QCM-D and fluorescence images (Fig. 3, *c*–*e*), yet the bilayer continuity was maintained, as highlighted by the full recovery in FRAP (Fig. 3, *c*–*e*). The single pore conductance shows that HNP1 forms transmembrane pores (Fig. 4 *e*), as it has been previously reported (87) and further supported by solid NMR, in which HNP1 dimers line the pore with the hydrophilic part of the peptide facing the water column (88). However, their total pore size observed by EIS (Fig. 4 *b*) was 1.6 μm^2 at 29 μM, which corresponds to $1.7 \times 10^{-6}\%$ of the total lipid bilayer area, implying that the pore formation might be only a minor function of HNP1. When LL-37 and HNP1 were mixed, both the destruction of bilayers induced by LL-37 and the membrane protrusion induced by HNP1 were inhibited, as seen by a lack of significant mass change in QCM-D (Fig. 3 *e*; Fig. S2), full recovery in FRAP (Fig. 3, *c* and *d*), and only minor defects or pores observed by EIS and transmembrane conductance (Fig. 4, *a*–*e*). Cryo-TEM demonstrated bilayer sheets and objects that resemble nanodisks, which also support that mixing HNP1 partially suppressed the destruction of bilayers by LL-37 because LL-37 alone fragmented vesicles into much smaller particles.

These functional studies demonstrated that the cooperative activities of LL-37 and HNP1 start only in lipid bilayers. Both LL-37 and HNP1 form homo-oligomers in aqueous solution without binding each other, yet upon incorporation into bilayers, the unique hydrophobic environment triggers their interactions and initiates the cooperative effect (Fig. 6). To further link the function to the structure, a set of additional experiments were performed by CD and fluorescence spectroscopy. When LL-37 was titrated by POPC vesicles, the amount of helix in LL-37 increased as the intensity of the double-dip structure became enhanced as a function of lipid to peptide ratio (L:P) until it reached saturation at L:P = 10 (Fig. S5 *a*). The ratio between the dip at 222 and 208 nm (CD222/CD208), which has been previously associated with the aggregation of the peptides (89), did not change significantly as a function of L/P ratio. When we titrated the mixture of LL-37 and HNP1 by POPC vesicles, a similar result was obtained (Fig. S5 *b*), implying that the secondary structure of LL-37 was not significantly altered by the presence of HNP1 in bilayers. Next, we monitored the titration by fluorescence spectroscopy to follow the emission spectra from the solvatochromic tryptophan in HNP1. When HNP1 was titrated by POPC vesicles, a blue shift was observed, suggesting that the tryptophan is in contact with the hydrophobic carbon chains in lipids (Fig. S6). When the LL-37/HNP1 mixture was titrated by POPC vesicles, the emission spectra blue shifted similarly after the subtraction of the spectra from LL-37 (Fig. S6). This suggests that the exposure of the tryptophan, which is near the C-terminal of HNP1, to the lipid environment was also not altered by the presence of LL-37. This lack of clear evidence toward peptide-peptide interactions in membranes suggests that the observed cooperative function might originate from a lipid-mediated interaction without strong direct peptide-peptide contact.

In conclusion, we report that LL-37 and HNP1 exhibited an unexpected antagonism that prevented LL-37

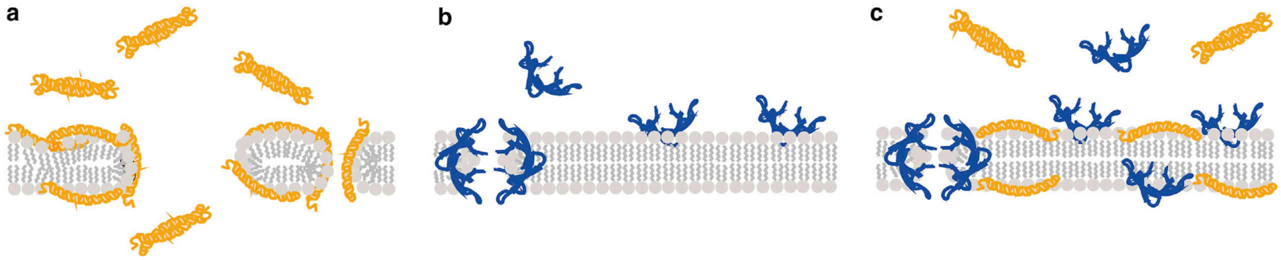

FIGURE 6 Schemes presenting the possible model of interactions between (*a*) LL-37, (*b*) HNP1, (*c*) LL-37 + HNP1, and POPC lipid bilayers. To see this figure in color, go online.

cytotoxicity in MDCK cells and HUVEC. LL-37 and HNP1 did not bind in physiological buffer solution, partially because their initial oligomeric states in solution concealed their hydrophobic residues, whereas their positive charge induced electric repulsion between them. The LL-37 binding to POPC bilayers was only moderately affected by the presence of HNP1. However, once they adhered to bilayers, this hydrophobic environment triggered their interactions and generated the cooperative effects, in which LL-37 could not destroy bilayers anymore. This explains the observed neutralization of cytotoxicity as LL-37-induced membrane destruction was the origin of the toxicity. These biophysics assays based on supported and pore-spanning bilayers used in this work (FRAP, EIS, QCM-D, and bilayer conductance measurements) in addition to other vesicle-based spectroscopy and ultrahigh-resolved cryo-imaging techniques are proven to be informative tools for studying the cooperative functions of AMPs.

SUPPORTING MATERIAL

Supporting Material can be found online at https://doi.org/10.1016/j.bpj.2020.10.031.

AUTHOR CONTRIBUTIONS

E.D. contributed to the design of the experiments, performed these experiments, analyzed data, and drafted the manuscript. K.S. contributed to the design of the experiments, analysis, and interpretation of the data and the drafting of the manuscript.

ACKNOWLEDGMENTS

We are grateful to Prof. Teresa Fitzpatrick, Prof. Eric Vauthey, Prof. Michal Borkovec, and Dr. Naomi Sakai from University of Geneva (Geneva, Switzerland) for kindly providing access to instruments. We thank Dr. Sebastian Glatt, Dr. Michal Rawski, and Dr. Paulina Indyka for support on performing three-dimensional tomography on Titan Krios microscope at SOLARIS National Synchrotron Radiation Centre (Cracow, Poland). We thank Dr. Mohamed Chami from Center for Cellular Imaging and NanoAnalytics (University of Basel, Basel, Switzerland) for sample preparation and image collection on FEI Talos microscope.

Part of the research leading to these results has received funding from Swiss National Foundation, the Swiss National Centre of Competence in Research Chemical Biology, Fondation Ernst et Lucie Schmidheiny, Leading House for the Middle East and North Africa (University of Applied Sciences and Arts Western Switzerland), the 2020 University of Tokyo Excellent Young Researcher, the Female Faculty Startup Grant, the special fund of Institute of Industrial Science (the University of Tokyo), Japan Society for the Promotion of Science KAKENHI grant JP20K22324, Naito Foundation and Kanamori Foundation.

REFERENCES

1. Westerhoff, H. V., M. Zasloff, …, D. Juretić. 1995. Functional synergism of the magainins PGLa and magainin-2 in *Escherichia coli*, tumor cells and liposomes. *Eur. J. Biochem.* 228:257–264.
2. Matsuzaki, K., Y. Mitani, …, K. Miyajima. 1998. Mechanism of synergism between antimicrobial peptides magainin 2 and PGLa. *Biochemistry.* 37:15144–15153.
3. Kobayashi, S., Y. Hirakura, and K. Matsuzaki. 2001. Bacteria-selective synergism between the antimicrobial peptides alpha-helical magainin 2 and cyclic beta-sheet tachyplesin I: toward cocktail therapy. *Biochemistry.* 40:14330–14335.
4. Cirioni, O., C. Silvestri, …, A. Giacometti. 2008. Protective effects of the combination of alpha-helical antimicrobial peptides and rifampicin in three rat models of *Pseudomonas aeruginosa* infection. *J. Antimicrob. Chemother.* 62:1332–1338.
5. Tang, Y. Q., M. R. Yeaman, and M. E. Selsted. 2002. Antimicrobial peptides from human platelets. *Infect. Immun.* 70:6524–6533.
6. Yan, H., and R. E. Hancock. 2001. Synergistic interactions between mammalian antimicrobial defense peptides. *Antimicrob. Agents Chemother.* 45:1558–1560.
7. Levy, O., C. E. Ooi, …, P. Elsbach. 1994. Individual and synergistic effects of rabbit granulocyte proteins on *Escherichia coli*. *J. Clin. Invest.* 94:672–682.
8. Rosenfeld, Y., D. Barra, …, M. L. Mangoni. 2006. A synergism between temporins toward Gram-negative bacteria overcomes resistance imposed by the lipopolysaccharide protective layer. *J. Biol. Chem.* 281:28565–28574.
9. Nuding, S., T. Frasch, …, L. T. Zabel. 2014. Synergistic effects of antimicrobial peptides and antibiotics against *Clostridium difficile*. *Antimicrob. Agents Chemother.* 58:5719–5725.
10. Nagaoka, I., S. Hirota, …, M. Hirata. 2000. Synergistic actions of antibacterial neutrophil defensins and cathelicidins. *Inflamm. Res.* 49:73–79.
11. Lüders, T., G. A. Birkemo, …, I. F. Nes. 2003. Strong synergy between a eukaryotic antimicrobial peptide and bacteriocins from lactic acid bacteria. *Appl. Environ. Microbiol.* 69:1797–1799.
12. Lauth, X., J. J. Babon, …, M. E. Westerman. 2005. Bass hepcidin synthesis, solution structure, antimicrobial activities and synergism, and in vivo hepatic response to bacterial infections. *J. Biol. Chem.* 280:9272–9282.
13. Wang, Z., L. Zhang, …, A. Shan. 2014. Synergistic interaction of PMAP-36 and PRW4 with aminoglycoside antibiotics and their antibacterial mechanism. *World J. Microbiol. Biotechnol.* 30:3121–3128.
14. Xiang, J., M. Zhou, …, L. Wang. 2017. The synergistic antimicrobial effects of novel bombinin and bombinin H peptides from the skin secretion of *Bombina orientalis*. *Biosci. Rep.* 37:BSR20170967.
15. Zheng, Z., N. Tharmalingam, …, E. Mylonakis. 2017. Synergistic efficacy of Aedes aegypti antimicrobial peptide cecropin A2 and tetracycline against Pseudomonas aeruginosa. *Antimicrob Agents Chemother.* 61:e00686-17.
16. Marxer, M., V. Vollenweider, and P. Schmid-Hempel. 2016. Insect antimicrobial peptides act synergistically to inhibit a trypanosome parasite. *Philos. Trans. R Soc. Lond. B Biol. Sci.* 371:20150302.
17. Svensson, D., J. O. Lagerstedt, …, R. Del Giudice. 2017. Apolipoprotein A-I attenuates LL-37-induced endothelial cell cytotoxicity. *Biochem. Biophys. Res. Commun.* 493:71–76.
18. Yang, A., C. Wang, …, C. Wang. 2017. Attenuation of β-amyloid toxicity in vitro and in vivo by accelerated aggregation. *Neurosci. Bull.* 33:405–412.
19. De Lorenzi, E., M. Chiari, …, A. E. Barron. 2017. Evidence that the human innate immune peptide LL-37 may be a binding partner of amyloid-β and inhibitor of fibril assembly. *J. Alzheimers Dis.* 59:1213–1226.
20. Williams, R. W., R. Starman, …, D. Covell. 1990. Raman spectroscopy of synthetic antimicrobial frog peptides magainin 2a and PGLa. *Biochemistry.* 29:4490–4496.
21. Tremouilhac, P., E. Strandberg, …, A. S. Ulrich. 2006. Synergistic transmembrane alignment of the antimicrobial heterodimer PGLa/magainin. *J. Biol. Chem.* 281:32089–32094.

22. Salnikov, E. S., and B. Bechinger. 2011. Lipid-controlled peptide topology and interactions in bilayers: structural insights into the synergistic enhancement of the antimicrobial activities of PGLa and magainin 2. *Biophys. J.* 100:1473–1480.

23. Nishida, M., Y. Imura, …, K. Matsuzaki. 2007. Interaction of a magainin-PGLa hybrid peptide with membranes: insight into the mechanism of synergism. *Biochemistry.* 46:14284–14290.

24. Zerweck, J., E. Strandberg, …, A. S. Ulrich. 2017. Molecular mechanism of synergy between the antimicrobial peptides PGLa and magainin 2. *Sci. Rep.* 7:13153.

25. Han, E., and H. Lee. 2015. Synergistic effects of magainin 2 and PGLa on their heterodimer formation, aggregation, and insertion into the bilayer. *Rsc Adv.* 5:2047–2055.

26. Agerberth, B., H. Gunne, …, G. H. Gudmundsson. 1995. FALL-39, a putative human peptide antibiotic, is cysteine-free and expressed in bone marrow and testis. *Proc. Natl. Acad. Sci. USA.* 92:195–199.

27. Ganz, T. 2003. Defensins: antimicrobial peptides of innate immunity. *Nat. Rev. Immunol.* 3:710–720.

28. Rodríguez-García, M., H. Oliva, …, T. Gallart. 2007. Human immature monocyte-derived dendritic cells produce and secrete alpha-defensins 1-3. *J. Leukoc. Biol.* 82:1143–1146.

29. Agerberth, B., J. Charo, …, G. H. Gudmundsson. 2000. The human antimicrobial and chemotactic peptides LL-37 and alpha-defensins are expressed by specific lymphocyte and monocyte populations. *Blood.* 96:3086–3093.

30. Chalifour, A., P. Jeannin, …, Y. Delneste. 2004. Direct bacterial protein PAMP recognition by human NK cells involves TLRs and triggers alpha-defensin production. *Blood.* 104:1778–1783.

31. Johansson, J., G. H. Gudmundsson, …, B. Agerberth. 1998. Conformation-dependent antibacterial activity of the naturally occurring human peptide LL-37. *J. Biol. Chem.* 273:3718–3724.

32. Sugihara, K., J. Vörös, and T. Zambelli. 2010. A gigaseal obtained with a self-assembled long-lifetime lipid bilayer on a single polyelectrolyte multilayer-filled nanopore. *ACS Nano.* 4:5047–5054.

33. Sugihara, K., J. Vörös, and T. Zambelli. 2010. The resistance of polyelectrolyte multilayers in a free-hanging configuration. *J. Phys. Chem. B.* 114:13982–13987.

34. Sugihara, K., M. Delai, …, T. Zambelli. 2012. Simultaneous OWLS and EIS monitoring of supported lipid bilayers with the pore forming peptide melittin. *Sens. Actuators B Chem.* 161:600–606.

35. Sugihara, K., B. Jang, …, T. Zambelli. 2012. A universal method for planar lipid bilayer formation by freeze and thaw. *Soft Matter.* 8:5525–5531.

36. Tsemperouli, M., and K. Sugihara. 2018. Characterization of di-4-ANEPPS with nano-black lipid membranes. *Nanoscale.* 10:1090–1098.

37. Lee, L. M., M. Tsemperouli, …, S. Matile. 2019. Anion transport with pnictogen bonds in direct comparison with chalcogen and halogen bonds. *J. Am. Chem. Soc.* 141:810–814.

38. Tsemperouli, M., E. Amstad, …, K. Sugihara. 2019. Black lipid membranes: challenges in simultaneous quantitative characterization by electrophysiology and fluorescence microscopy. *Langmuir.* 35:8748–8757.

39. Duplantier, A. J., and M. L. van Hoek. 2013. The human cathelicidin antimicrobial peptide LL-37 as a potential treatment for polymicrobial infected wounds. *Front. Immunol.* 4:143.

40. Kai-Larsen, Y., and B. Agerberth. 2008. The role of the multifunctional peptide LL-37 in host defense. *Front. Biosci.* 13:3760–3767.

41. Gambade, A., S. Zreika, …, G. Weber. 2016. Activation of TRPV2 and BKCa channels by the LL-37 enantiomers stimulates calcium entry and migration of cancer cells. *Oncotarget.* 7:23785–23800.

42. Ramos, R., J. P. Silva, …, M. Gama. 2011. Wound healing activity of the human antimicrobial peptide LL37. *Peptides.* 32:1469–1476.

43. Oudhoff, M. J., M. E. Blaauboer, …, E. C. Veerman. 2010. The role of salivary histatin and the human cathelicidin LL-37 in wound healing and innate immunity. *Biol. Chem.* 391:541–548.

44. Lau, Y. E., D. M. Bowdish, …, D. J. Davidson. 2006. Apoptosis of airway epithelial cells: human serum sensitive induction by the cathelicidin LL-37. *Am. J. Respir. Cell Mol. Biol.* 34:399–409.

45. Tomasinsig, L., C. Pizzirani, …, M. Zanetti. 2008. The human cathelicidin LL-37 modulates the activities of the P2X7 receptor in a structure-dependent manner. *J. Biol. Chem.* 283:30471–30481.

46. Avitabile, C., L. D. D'Andrea, and A. Romanelli. 2014. Circular Dichroism studies on the interactions of antimicrobial peptides with bacterial cells. *Sci. Rep.* 4:4293.

47. Seelig, J. 2004. Thermodynamics of lipid-peptide interactions. *Biochim. Biophys. Acta.* 1666:40–50.

48. Wenk, M. R., and J. Seelig. 1998. Magainin 2 amide interaction with lipid membranes: calorimetric detection of peptide binding and pore formation. *Biochemistry.* 37:3909–3916.

49. Vaz, W. L., R. M. Clegg, and D. Hallmann. 1985. Translational diffusion of lipids in liquid crystalline phase phosphatidylcholine multibilayers. A comparison of experiment with theory. *Biochemistry.* 24:781–786.

50. Johannsmann, D., K. Mathauer, …, W. Knoll. 1992. Viscoelastic properties of thin films probed with a quartz-crystal resonator. *Phys. Rev. B Condens. Matter.* 46:7808–7815.

51. Wang, K. F., R. Nagarajan, and T. A. Camesano. 2015. Differentiating antimicrobial peptides interacting with lipid bilayer: molecular signatures derived from quartz crystal microbalance with dissipation monitoring. *Biophys. Chem.* 196:53–67.

52. Lind, T. K., and M. Cárdenas. 2016. Understanding the formation of supported lipid bilayers via vesicle fusion-A case that exemplifies the need for the complementary method approach (Review). *Biointerphases.* 11:020801.

53. Keller, C. A., and B. Kasemo. 1998. Surface specific kinetics of lipid vesicle adsorption measured with a quartz crystal microbalance. *Biophys. J.* 75:1397–1402.

54. Cremer, P. S., and S. G. Boxer. 1999. Formation and spreading of lipid bilayers on planar glass supports. *J. Phys. Chem. B.* 103:2554–2559.

55. Voinova, M. V., M. Rodahl, …, B. Kasemo. 1999. Viscoelastic acoustic response of layered polymer films at fluid-solid interfaces: continuum mechanics approach. *Phys. Scr.* 59:391–396.

56. Mechler, A., S. Praporski, …, L. L. Martin. 2007. Specific and selective peptide-membrane interactions revealed using quartz crystal microbalance. *Biophys. J.* 93:3907–3916.

57. Wang, K. F., R. Nagarajan, …, T. A. Camesano. 2011. Characterization of supported lipid bilayer disruption by chrysophsin-3 using QCM-D. *J. Phys. Chem. B.* 115:15228–15235.

58. Nirschl, M., M. Schreiter, and J. Vörös. 2011. Comparison of FBAR and QCM-D sensitivity dependence on adlayer thickness and viscosity. *Sens. Actuators A Phys.* 165:415–421.

59. Zhang, X., K. Oglęcka, …, A. Gräslund. 2010. Dual functions of the human antimicrobial peptide LL-37-target membrane perturbation and host cell cargo delivery. *Biochim. Biophys. Acta.* 1798:2201–2208.

60. Oren, Z., and Y. Shai. 1998. Mode of action of linear amphipathic alpha-helical antimicrobial peptides. *Biopolymers.* 47:451–463.

61. Lin, J., M. Merzlyakov, …, P. C. Searson. 2008. Impedance spectroscopy of bilayer membranes on single crystal silicon. *Biointerphases.* 3:FA33.

62. Nikolov, V., J. Lin, …, P. C. Searson. 2007. Electrical measurements of bilayer membranes formed by Langmuir-Blodgett deposition on single-crystal silicon. *Langmuir.* 23:13040–13045.

63. Purrucker, O., H. Hillebrandt, …, M. Tanaka. 2001. Deposition of highly resistive lipid bilayer on silicon-silicon dioxide electrode and incorporation of gramicidin studied by ac impedance spectroscopy. *Electrochim. Acta.* 47:791–798.

64. Eichmann, C., S. Campioni, …, R. Riek. 2016. Preparation and characterization of stable α-synuclein lipoprotein particles. *J. Biol. Chem.* 291:8516–8527.

65. Denisov, I. G., Y. V. Grinkova, …, S. G. Sligar. 2004. Directed self-assembly of monodisperse phospholipid bilayer nanodiscs with controlled size. *J. Am. Chem. Soc.* 126:3477–3487.

66. Xu, X. P., D. Zhai, …, D. Hanein. 2013. Three-dimensional structure of Bax-mediated pores in membrane bilayers. *Cell Death Dis.* 4:e683.

67. Bergman, P., L. Walter-Jallow, …, J. Söderlund. 2007. The antimicrobial peptide LL-37 inhibits HIV-1 replication. *Curr. HIV Res.* 5:410–415.

68. Wu, W. K., G. Wang, …, C. H. Cho. 2010. Emerging roles of the host defense peptide LL-37 in human cancer and its potential therapeutic applications. *Int. J. Cancer.* 127:1741–1747.

69. Barlow, P. G., Y. Li, …, D. J. Davidson. 2006. The human cationic host defense peptide LL-37 mediates contrasting effects on apoptotic pathways in different primary cells of the innate immune system. *J. Leukoc. Biol.* 80:509–520.

70. Yu, J., N. Mookherjee, …, R. E. Hancock. 2007. Host defense peptide LL-37, in synergy with inflammatory mediator IL-1beta, augments immune responses by multiple pathways. *J. Immunol.* 179:7684–7691.

71. Vandamme, D., B. Landuyt, …, L. Schoofs. 2012. A comprehensive summary of LL-37, the factotum human cathelicidin peptide. *Cell. Immunol.* 280:22–35.

72. Heilborn, J. D., M. F. Nilsson, …, M. Ståhle-Bäckdahl. 2003. The cathelicidin anti-microbial peptide LL-37 is involved in re-epithelialization of human skin wounds and is lacking in chronic ulcer epithelium. *J. Invest. Dermatol.* 120:379–389.

73. Ganz, T., M. E. Selsted, …, R. I. Lehrer. 1985. Defensins. Natural peptide antibiotics of human neutrophils. *J. Clin. Invest.* 76:1427–1435.

74. Mandal, M., and R. Nagaraj. 2002. Antibacterial activities and conformations of synthetic alpha-defensin HNP-1 and analogs with one, two and three disulfide bridges. *J. Pept. Res.* 59:95–104.

75. Wilson, S. S., M. E. Wiens, and J. G. Smith. 2013. Antiviral mechanisms of human defensins. *J. Mol. Biol.* 425:4965–4980.

76. Kim, C., N. Gajendran, …, S. H. E. Kaufmann. 2005. Human alpha-defensins neutralize anthrax lethal toxin and protect against its fatal consequences. *Proc. Natl. Acad. Sci. USA.* 102:4830–4835.

77. Yang, D., Z. H. Liu, …, J. J. Oppenheim. 2007. Defensin participation in innate and adaptive immunity. *Curr. Pharm. Des.* 13:3131–3139.

78. den Hertog, A. L., J. van Marle, …, A. V. Nieuw Amerongen. 2005. Candidacidal effects of two antimicrobial peptides: histatin 5 causes small membrane defects, but LL-37 causes massive disruption of the cell membrane. *Biochem. J.* 388:689–695.

79. Lehrer, R. I., T. Ganz, …, M. E. Selsted. 1988. Modulation of the in vitro candidacidal activity of human neutrophil defensins by target cell metabolism and divalent cations. *J. Clin. Invest.* 81:1829–1835.

80. Ding, J., Y. Y. Chou, and T. L. Chang. 2009. Defensins in viral infections. *J. Innate Immun.* 1:413–420.

81. Li, Y., X. Li, …, G. Wang. 2007. A novel method for purifying recombinant human host defense cathelicidin LL-37 by utilizing its inherent property of aggregation. *Protein Expr. Purif.* 54:157–165.

82. Oren, Z., J. C. Lerman, …, Y. Shai. 1999. Structure and organization of the human antimicrobial peptide LL-37 in phospholipid membranes: relevance to the molecular basis for its non-cell-selective activity. *Biochem. J.* 341:501–513.

83. Xhindoli, D., S. Pacor, …, A. Tossi. 2014. Native oligomerization determines the mode of action and biological activities of human cathelicidin LL-37. *Biochem. J.* 457:263–275.

84. Pazgier, M., G. Wei, …, W. Lu. 2012. Sometimes it takes two to tango: contributions of dimerization to functions of human α-defensin HNP1 peptide. *J. Biol. Chem.* 287:8944–8953.

85. Henzler Wildman, K. A., D. K. Lee, and A. Ramamoorthy. 2003. Mechanism of lipid bilayer disruption by the human antimicrobial peptide, LL-37. *Biochemistry.* 42:6545–6558.

86. Neville, F., M. Cahuzac, …, D. Gidalevitz. 2006. Lipid headgroup discrimination by antimicrobial peptide LL-37: insight into mechanism of action. *Biophys. J.* 90:1275–1287.

87. Kagan, B. L., M. E. Selsted, …, R. I. Lehrer. 1990. Antimicrobial defensin peptides form voltage-dependent ion-permeable channels in planar lipid bilayer membranes. *Proc. Natl. Acad. Sci. USA.* 87:210–214.

88. Zhang, Y., W. Lu, and M. Hong. 2010. The membrane-bound structure and topology of a human α-defensin indicate a dimer pore mechanism for membrane disruption. *Biochemistry.* 49:9770–9782.

89. Lau, S. Y., A. K. Taneja, and R. S. Hodges. 1984. Synthesis of a model protein of defined secondary and quaternary structure. Effect of chain length on the stabilization and formation of two-stranded alpha-helical coiled-coils. *J. Biol. Chem.* 259:13253–13261.

Biophysical Journal, Volume *119*

Supplemental Information

Cooperative Function of LL-37 and HNP1 Protects Mammalian Cell Membranes from Lysis

Ewa Drab and Kaori Sugihara

Contents

Supporting Figures

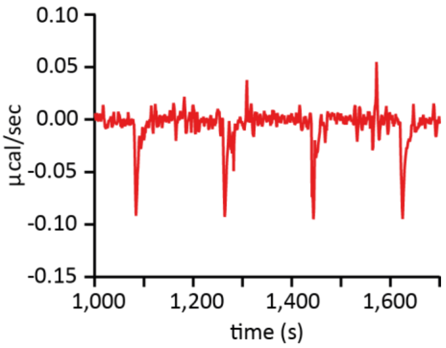

Figure S1 Reverse titration in isothermal titration calorimetry (ITC). 15 mM POPC vesicles were titrated with 100 µM LL-37 at 2 µl for each injection. During this reverse titration lipids are in excess compared to peptides, yielding an equal amount of heat at each injection. The binding enthalpy per 1 mol of peptide estimated from this reverse titration (-5.57 kcal/mol) is in agreement with that from the standard lipid-into-peptide titration shown in Fig. 3a in the main text (-5.73 kcal/mol). This validates the analysis of ITC for extracting entropy and enthalpy shown in the text. The experiment was performed in a physiological HEPES buffer solution (10 mM HEPES, 150 mM NaCl, pH = 7.4).

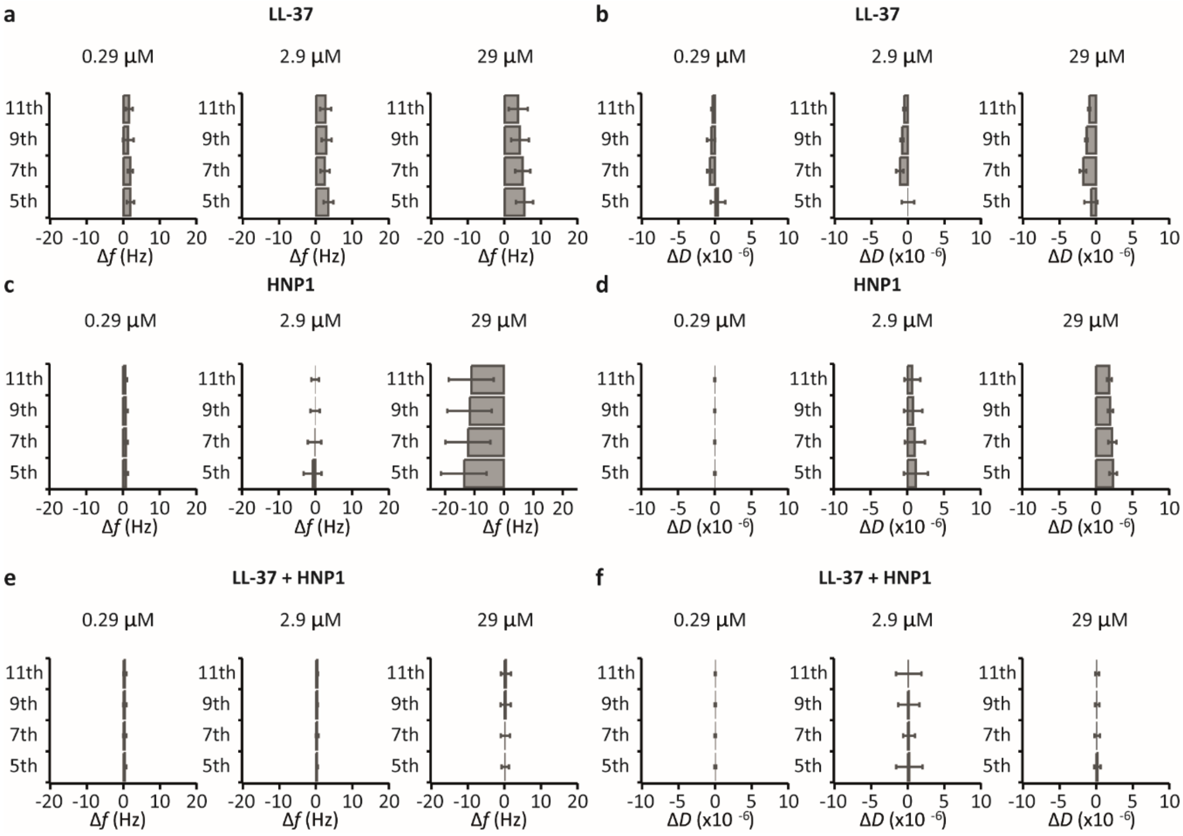

Figure S2 Overtone analysis of the quartz crystal microbalance (QCM) experiment shown in Fig. 3e in the main text.

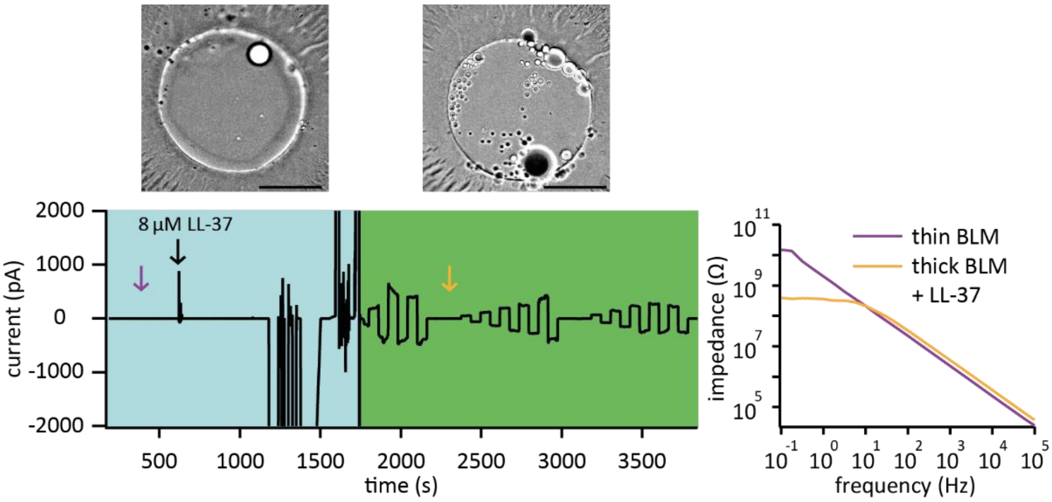

Figure S3 Comparison of conductance measurements at a fixed voltage and impedance spectra taken in between. During this experiment, the bilayer thickened from 3.0 nm to 10.4 nm as the impedance spectra taken at the beginning (purple) and in the middle (yellow) indicate a decrease in the capacitance. Nevertheless, the transmembrane conductance remained even after the bilayer thickened. Scale bar 50 μm.

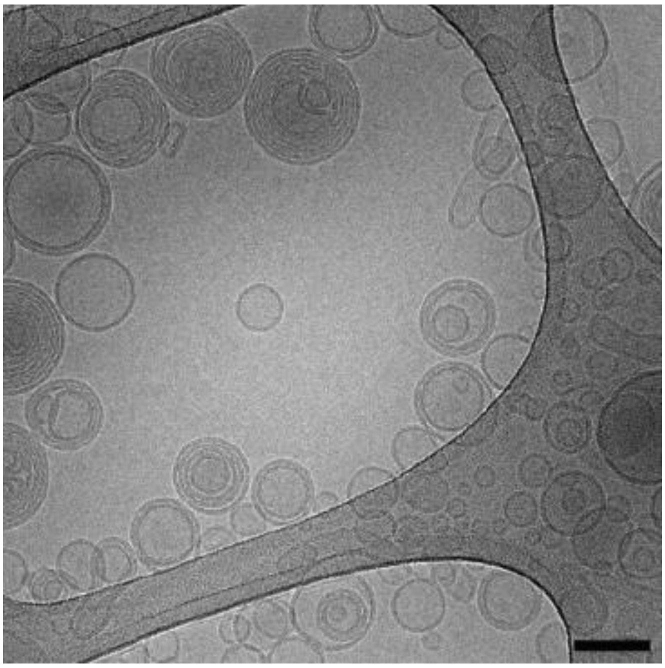

Figure S4 A cryo-transmission electron microscopy (cryo-TEM) image of POPC vesicles. Scale bar 100 nm.

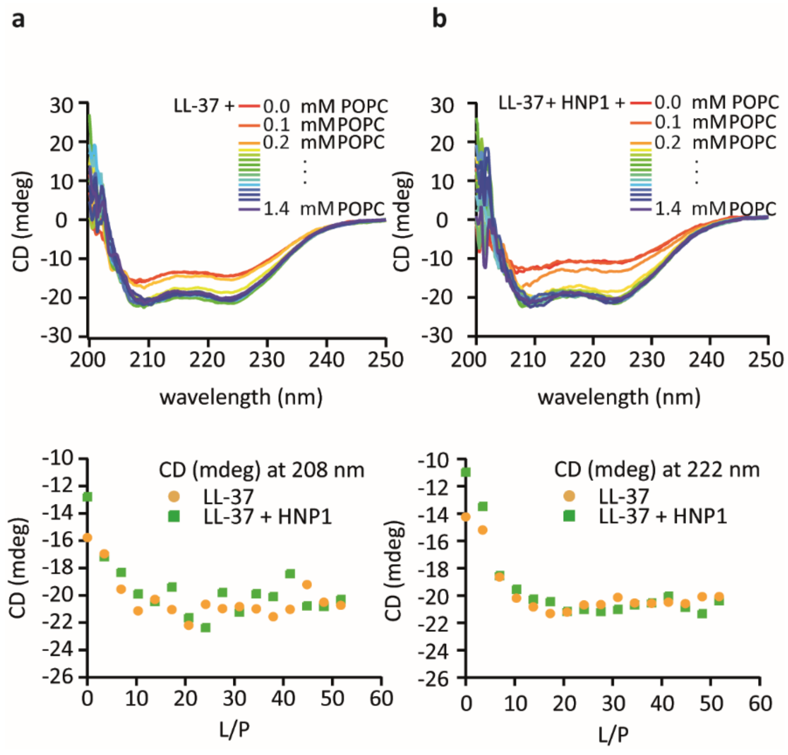

Figure S5 CD spectra of (a) LL-37 alone and (b) in pair with HNP1 titrated with POPC vesicles and the corresponding analysis of the intensity at 208 nm and 222 nm as a function of lipid-to-peptide ratio. 29 μM of LL-37 or LL-37 + HNP1 (58 μM at a final concentration) was titrated with 15 mM of POPC vesicles at 2 μl for each injection. The last injection corresponds to the final POPC concentration at 1.4 mM. For the spectra of LL-37 + HNP1 mixture in solution, the spectra of HNP1 alone in solution is subtracted. For the spectra of LL-37 + HNP1 mixture in vesicles, the spectra of HNP1 in vesicles at the corresponding lipid-to-peptide ratio is subtracted. No significant difference was observed between LL-37 and LL-37 + HNP1 mixture. The experiment was performed in a physiological HEPES buffer solution (10 mM HEPES, 150 mM NaCl, pH=7.4).

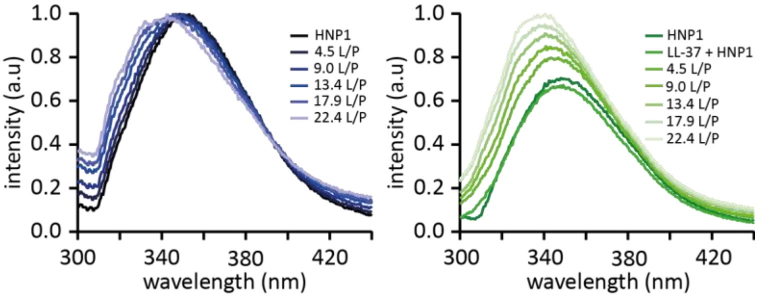

Figure S6 Fluorescence emission of Trp residue in HNP1 measured during the titration with POPC vesicles with or without LL-37. HNP1 or its mixture with LL-37 at 2.9 µM (in case of mixture 2.9 µM HNP1 + 2.9 µM LL-37) were titrated with POPC vesicles at 1.3 mM with 4 µl for each injection. The experiments were performed in 10 mM HEPES buffer solution with 150 mM NaCl, pH = 7.4.

METHODS

Materials

HEPES buffer solution was prepared with 10 mM 4-(2-hydroxyethyl) piperazine-1-ethanesulfonic acid (HEPES, Fluka, Switzerland) with addition of either 150 mM sodium chloride (Sigma Aldrich, Switzerland) or 2 M potassium chloride (Sigma Aldrich, Switzerland) in ultra-pure water filtered through MilliQ Gradient A10 filters (Millipore AG, Switzerland). The pH was adjusted to 7.4 using 6M NaOH (Sigma Aldrich, Switzerland). Prior to use, buffer was sterile filtered through 0.22 µm pore size PVDF membrane (Merck, Switzerland). 1-palmitoyl-2-oleoyl-*sn*-glycero-3-phosphocholine (POPC, #850457) and 1,2-dioleoyl-sn-glycero-3-phosphoethanolamine-N-(7-nitro-2-1,3-benzoxadiazol-4-yl) (ammonium salt) (NBDPE, #810145) were purchased from Avanti Polar Lipids. n-decane (reagent plus ≥ 99%) and hexane (reagent plus ≥ 99%) were purchased from Sigma Aldrich (Germany). Fluo-3 AM FluoroPure^{TM} grade (Invitrogen, #F23917) were purchased from Thermo Fischer Scientific. Human Neutrophil Peptide-1 (HNP1, #4025473) was purchased from Bachem (Switzerland), while Human LL-37 Cathelicidin (LL-37, #AM-001) was purchased from IscaBiochemicals (United Kingdom). Both peptides were dissolved and stored according to instructions provided by the manufacturers.

Cell culture

Primary Human Umbilical Vein Endothelial Cells (HUVEC) from pooled donors, proliferating, were purchased from PromoCell (PromoCell, #12253) and cultured in complete Phenol-red free (PRF) medium (PromoCell, #C-22215 supplemented with Growth Medium supplementPack, #C-39210) according to manufacturer’s instructions. Madin-Darby Canine Kidney (MDCK) cells were a gift from Prof. Aurélien Roux (University of Geneva) and cultured in high glucose

DMEM Glutamax^{TM} (Gibco, #61965), supplemented with 10% fetal calf serum (Bioconcept, Switzerland, #2-01F10-I) and 1% penicillin streptomycin (Gibco, #15140122).

Intracellular calcium response monitored with Fluo-3 indicator

The cells were loaded with membrane permeable ester of calcium indicator Fluo-3 AM, which upon entry into the cytosol undergoes hydrolysis by intracellular enzymes into membrane impermeable form. After loading into the cells in the dark and leaving the culture dish for 40 min to reach the cells quiescence, the time lapse imaging was performed at 37 °C by a confocal laser scanning microscope (CLSM, confocal A1, Nikon, Japan) with an oil immersion objective (CFI PLAN APO LBDA 60X, Nikon, Japan). The microscope is integrated with perfect focus system, active vibration isolation platform (i4 series, Accurion, Germany) and an acoustic enclosure equipped with a temperature controller (JPK Instruments, Germany). After taking some frames without peptide, the AMPs were added either individually or in a pair at a final concentration of 29 µM, and the time-lapse images were recorded. To monitor changes in fluorescence of Fluo-3 indicator, 488 nm laser excitation wavelength and a FITC A1 emission filter (525/50) were selected. Images were taken with 1024 pixels resolution and were further analyzed with ImageJ software.

Isothermal Titration Calorimetry (ITC)

POPC dissolved in chloroform was dried under a stream of nitrogen and left in a vacuum overnight for completely removing the organic solvent residuals. Obtained lipid films were rehydrated in buffer solution (10 mM HEPES, 150 mM NaCl, pH=7.4) at a final concentration of 15 mM, left for 2h and went through high power titanium tip sonicator treatment (Omni Sonic Ruptor 400 Ultrasonic Homogenizer, Omni International) until solution became transparent, followed by ultracentrifugation to separate titanium particles from the vesicle solution. The measurements were carried out on VP-ITC Microcalorimeter (MicroCal. Inc., Northampton, MA) with a chamber volume of 200 µl. Prior to each experiment, the sample cell was cleaned following the manufacturer's protocol. To investigate peptide-peptide interaction in aqueous solution, 40 µM HNP1 was titrated with 400 µM LL-37 peptide and heats of reaction were recorded. To account for heats of dilution, control experiment was performed, where 400 µM LL-37 was titrated into a buffer solution, and the result was subtracted from the data presented in Fig. 2. For the lipid to peptide titration in Fig. 3, relevant peptide solution at a final concentration of 40 µM in 10 mM HEPES, 150 mM NaCl was placed in the sample cell and left to equilibrate for 30 min at 25°C. POPC vesicle solution was loaded into an injection syringe with a purge and re-fill procedure in order to dislodge any air bubbles remaining in the syringe. During the experiment 2 µl vesicle suspension was injected into stirred peptide solution with 180 s intervals, at the reference power set to 6 µcal/sec, and the resulting heat change was measured. As a control experiment, to account for heats of dilution, vesicle solution was injected into a buffer solution without peptide, and this result was subtracted from the data shown in Fig. 3. In a separate experiment in Fig. S1, the reverse titration was performed, where peptides (100 µM LL-37) were injected into lipid vesicle suspension (15 mM POPC) with the same conditions as mentioned above. The binding enthalpy per 1 mol of peptide was calculated after subtraction of heat from a control experiment, where LL-37 was injected into a buffer solution. Data processing (baseline subtraction, peak integration, correction for sample dilution) was performed with MicroCal Origin software. Vesicle size and polydispersity index (PDI) were determined by dynamic light scattering (DLS) using Zetasizer Nano series (Nano-ZS, Malvern Panalytical) right after the ITC measurements. All the experiments were performed in HEPES buffer solution (10 mM HEPES, 150mM NaCl, pH = 7.4).

Circular Dichroism (CD) spectroscopy

CD spectra were recorded with a Jasco CD-J-815 spectropolarimeter using a quartz cuvette with path length of 1 mm. Each CD spectrum was recorded from 240 nm to 190 nm with 50 nm/min scanning speed, 1 nm bandwidth, 4 sec digital integration time at 25 °C at least for 10 times to improve the signal to noise ratio by averaging. Peptides at 29 µM were incubated in HEPES buffer solution (10 mM HEPES, 150 mM NaCl, pH = 7.4) for 1 h before measurement at 25 °C. For studying the secondary structure of peptides in solution, first the spectra for LL-37 and HNP1 were separately measured. Next, they were mixed at the final concentration of 29 µM for each, left for 1 h to stabilize and the spectra was taken. In Fig. 2c the spectra from LL-37 and LL-37 + HNP1 are shown, where for the mixture spectra from HNP1 is subtracted. For studying the secondary structure of peptides in vesicles, first the spectra from LL-37 in HEPES buffer solution was taken, followed by a sequential injection of 2 µl 15 mM POPC vesicle suspension prepared by sonication, where CD spectra was measured after each injection. The same procedure was repeated with HNP1 and the peptide mixture. LL-37 spectra and LL-37 + HNP1 spectra after the subtraction of HNP1 spectra at each concentration were presented in Fig. S5.

Fluorescence spectroscopy

The fluorescence emission spectra from Trp-26 residue in a hydrophobic region of HNP1 was measured before and after adding LL-37. Experiment was performed on FluoroMax-4 Spectrofluorometer (Horiba Scientific) with 280 nm excitation wavelength, emission between 300 to 500 nm, 1 nm step size and 5 nm excitation and emission slit widths in cuvette with 10 mm path length. Prior to measurement, HNP1 was dissolved in HEPES buffer solution (10 mM HEPES, 150 mM NaCl, pH = 7.4) at 2.9 µM and left 1h at 25 °C. After taking a spectrum, LL-37 was added at a final concentration of 2.9 µM and the spectra was collected every 5 minutes to monitor the possible time evolution of the signals. In addition, the effect of POPC lipid addition was monitored by injecting POPC vesicles every 5 minutes to HNP1 alone or in combination with LL-37 (Fig. S6).

Vesicle preparation for FRAP, QCM-D and EIS experiments

POPC and 0.2 % mol of NBD-PE dissolved in chloroform were mixed and dried under a stream of nitrogen and left in a vacuum overnight for completely removing the organic solvent residuals. Obtained lipid films were rehydrated in a buffer solution (10 mM HEPES, 150 mM NaCl, pH=7.4) at a final concentration of 1 mg/ml POPC, left for 2h and extruded for 31 cycles through two 50 nm polycarbonate membranes (Whatman Nuclepore Track-Etched Membranes, #800308) at room temperature to make small unilamellar vesicles (SUV).

Fluorescent Recovery After Photobleaching (FRAP)

Glass coverslips were cleaned in a bath sonicator with acetone followed by ethanol and MilliQ water, dried under nitrogen flow and activated in an oxygen plasma cleaner (TePla IoN 3MHz Plasma System, Germany) for 30 min. To form supported lipid bilayers, activated glass surface was incubated with the vesicle suspension for at least 20 min followed by extensive rinsing with buffer solution to eliminate any remained fluorescence vesicles. To study the influence of peptides on membrane lateral fluidity, individual types of peptides or their mixture were added at 2.9 μM and the supported lipid bilayers were incubated for 40 min followed by rinse. Time-lapse images were taken using Nikon Eclipse Ti-E inverted fluorescence microscope (Nikon, Japan) with 60x/1.40 oil-immersion objective (Plan Apo, Nikon). The microscope was equipped with a CCD camera (DS-Qi2, Nikon) and 482/35 excitation (nm) and 536/40 emission filters (nm) were used. The contrast and the brightness were adjusted and the images were presented with false colors in the figures. Diffusion coefficients were extracted based on double normalization presented elsewhere(1).

Quartz Crystal Microbalance with Dissipation Monitoring (QCM-D)

QCM-D measurements were performed with Q-SENSE (Biolin Scientific, Sweden) instrument by using Quartz Crystal, 5 Hz, AT cut, Gold electrode with 300 nm silicon-dioxide coating (QS-QSX318, Biolin Scientific, Sweden). Prior to use, these sensors were cleaned with 2% SDS, rinsed with ultrapure water (MilliQ), dried under a nitrogen stream and activated with an UV/ozone cleaner for 20 minutes. In order to investigate the mass and the viscoelastic properties, changes in resonance frequency and energy dissipation were recorded in real-time at four overtones of the fundamental resonance frequency at 25 °C. After the bilayer formation, peptides were injected sequentially at concentrations from 0.29 µM to 29 µM, where at each concentration bilayers were incubated with the peptides for 40 min and were rinsed with a buffer solution. The frequency and the dissipation shown in the overtone analysis in Fig. S2 are the changes between the signal after forming a lipid bilayer and that after rinse at each peptide injection normalized to overtones.

Electrochemical impedance spectroscopy (EIS)

Prior to use, highly conductive (0.001-0.005 Ω·cm) boron-doped (p-type) silicon wafers (University Wafer Inc.) with orientation <100> were cut into approximately 1 cm x 3 cm, cleaned with isopropanol, MilliQ water, and blow-dried with nitrogen. The electrode was mounted inside a half-home-made electrochemical chamber with a 3-electrode setup (Ag/AgCl as a reference and platinum as a counter electrode). The chamber volume is roughly 150 µl and an active working electrode area is around 0.95 cm^2. To form supported lipid bilayers over this silicon working electrodes, vesicles were injected into the flow cell immediately after extrusion and incubated for 2 h at room temperature, followed by rinse with a buffer solution. To trigger the vesicle rupture efficiently for forming defect-free bilayers with a resistance value in kΩ range, the highly conductive silicon wafers were activated with an oxygen plasma cleaner (TePla IoN 3MHz Plasma System) for 30 minutes immediately before the experiment. After the bilayer formation, peptides at the concentrations from 0.29 µM to 29 µM were injected into the flow cell sequentially, where at each concentration the bilayer was incubated for 40 minutes, rinsed with a buffer solution, and impedance spectra were measured with a 10 mV sinusoidal voltage at 0 V offset potential with Autolab PGSTAT302N (Metrohm, Switzerland). Obtained spectra were analyzed by Nova 1.11 Software (Metrohm, Switzerland) with an equivalent electrical circuit presented in Fig. 4a.

Impedance Spectroscopy data analysis

The measured data was analyzed after fitting with the following equivalent circuit R_{buffer} $(R_{\text{ch}}C_{\text{dl}})(R_{\text{LB}}C_{\text{LB}})$, where R_{buffer} represents a serial resistance of buffer solution, R_{ch} corresponds to charge transfer resistance and C_{dl} is the double layer capacitance. The bilayer formation is represented by an additional bilayer resistance R_{LB} and capacitance C_{LB}. The extracted bilayer resistance and capacitance were further converted into defect areas A_{defects} and bilayer thickness d_{LB}, respectively. First, the bilayer thickness was calculated. As a bilayer behaves like a capacitor, we could convert the capacitance values into bilayer thickness by using the following formula $C = \frac{\varepsilon_0 \varepsilon A'}{d_{\text{LB}}}$, where ε_0 is the space permittivity ($8.85 \cdot 10^{-12}$ F/m), ε is relative permittivity of the dielectric hydrocarbon region in lipid bilayers (2-4)(2, 3). A' is the area of the working electrode covered by lipid membrane (0.95 cm^2) and d_{LB} is the bilayer thickness.

For the calculations of the defect area A_{defect} the following equation was used:

$$A_{\mathrm{defect}} = \rho \frac{d_{\mathrm{LB}}}{R_{\mathrm{LB}}},$$

where ρ is the buffer resistivity (73.5 Ohm·cm)(4), d_{LB} is the membrane thickness (3.7 nm) and R_{LB} corresponds to the bilayer resistance.

Painting solution for conductance experiments

For the single channel conductance measurement lipid painting solution was prepared as follows: small volume of POPC lipids in chloroform was dried under nitrogen flow and left for two hours under vacuum to remove remaining solvent. Then, the lipids were re-suspended in 1:1 mixture of hexanes isomers and n-decane at a final concentration of 25 mg/ml, vortexed and used immediately in the conductance experiment.

Single Channel Conductance Experiment with Black Lipid Membranes (BLM)

The detail of the used homemade electrochemical chamber is described elsewhere (5). In brief, it contains two chambers (*cis* and *trans*) separated by a 25 µm thick Teflon sheet with a single pore (ø = 50-100 µm) that spans horizontally. This horizontal chamber design enables the optical microscopy to be coupled during the electrophysiological recordings. An Ag/AgCl electrode is connected to each chamber through an agar salt bridge (2-electrode setup). The whole chamber was filled with HEPES buffer solution (2M KCl, 10 mM HEPES, pH = 7.4). Painting solution (~ 2 µl) was brushed over the pore to form a black lipid membrane (BLM) and its spontaneous thinning was monitored by combining bright field microscopy (Nikon Eclipse Ts2R, Nikon, Japan) equipped with DS-Ri2 camera (Nikon, Japan) and impedance spectroscopy. When the estimated bilayer capacitance density (capacitance per area determined by the capacitance value extracted from the impedance spectroscopy divided by the bilayer area estimated from the bright field microscopy) was above 0.6 µF/cm^2 and the bilayer resistance was in GΩ range, further experiments were performed. Electrical measurement was recorded with an Autolab PGSTAT302N potentiostat equipped with a FRA32M and ECD Modules for low current detection. First, to monitor the incorporation of the peptides to the bilayers, peptides were added to the *cis* compartment, while keeping the voltage at 50 mV. Next, a voltage step sequence, 0 mV, 25 mV, -25 mV, 50 mV, -50 mV, 75 mV, -75 mV, 100 mV, -100 mV, 125 mV, -125 mV, 0 mV, where the potential was halt for 60 s at each potential was applied. The appearance of the bilayer was being monitored simultaneously by bright field microscopy. Before and after each voltage step sequence, impedance spectroscopy was performed to confirm membrane capacitance and resistance. Obtained impedance spectra were analyzed by Nova 1.11 Software (Metrohm, Switzerland).

For single channel current monitoring, the voltage was fixed at 50 mV or -125 mV (Fig. 4e) without voltage sweep. The obtained step currents I were expressed as a conductance g based on the Ohm’s law and were further converted into diameters by the following Hille equation(6):

$$g^{-1} = \frac{4 \cdot l \cdot \rho}{\pi \cdot d^2} + \frac{\rho}{d} ,$$

where g (= 50.4 pS) is the conductance from the single pore calculated from I, l (=3.7 nm) is the bilayer thickness, ρ (= 0.0481 Ωm) is the solution resistivity, from which the diameter of the single pore d was calculated.

Cryo-Electron Microscopy

Sample preparation: POPC lipids dissolved in chloroform were dried under nitrogen and left in desiccator for overnight, re-suspended in a buffer solution (10mM HEPES, 150mM NaCl, pH=7.4) at a final concentration of 15 mM, and filtered through 220 nm pore size membrane prior to use. Vesicles were prepared by 41 cycles of extrusion through two polycarbonate membranes with 100 nm pore size just before the experiment. Four samples were imaged: POPC vesicles, POPC vesicles incubated with LL-37, HNP1 and their 1:1 molar mixture. For the vesicle sample with peptides, POPC vesicles were incubated with each peptide or their mixture at the final vesicle concentration of 1.5 mM and the final LL-37 or HNP1 concentration of 150 μM, where in case of the mixture 150 μM of LL-37 and 150 μM of HNP1 were mixed, for 30 minutes at room temperature prior to vitrification. This makes the lipid to peptide ratio L/P=10 for the samples with individual peptides and 20 for that with peptide mixture.

Sample preparation for image acquisition with Krios G3i Cryo-EM

CryoEM grid (TED Pella 200 mesh 2x2) was treated with air plasma for 30 s and 10 mA current (Plasma Leica EM ACE 200). Then 4 μl of each sample was applied to the grid at 100% humidity, 1.5 s blot time, at 4 °C and vitrified in liquid ethane/nitrogen (Vitrobot, FEI).

Image acquisition: Frozen samples were imaged using Thermo Scientific Krios G3i Cryo-Transmission Electron Microscope (Cryo-TEM) operated at 300 kV. Samples were imaged in tomography mode from -60° to 60° every 2°.

Sample preparation for image acquisition with Talos Cryo-EM

CryoEM grid (Lacy Carbon Only TED PELLA) was treated with air plasma for 40 s. Then 4 μl of each sample was applied to the grid and vitrified at 90% humidity, 3 s blot time. Samples were imaged with FEI Talos Cryo-Transmission Electron Microscope operated at 200 kV with Ceta CMOS camera.

Supporting references

1. Phair, R. D., S. A. Gorski, and T. Misteli. 2004. Measurement of dynamic protein binding to chromatin in vivo, using photobleaching microscopy. Methods Enzymol 375:393-414.
2. Purrucker, O., H. Hillebrandt, K. Adlkofer, and M. Tanaka. 2001. Deposition of highly resistive lipid bilayer on silicon-silicon dioxide electrode and incorporation of gramicidin studied by ac impedance spectroscopy. Electrochim Acta 47(5):791-798.
3. Gritsch, S., P. Nollert, F. Jahnig, and E. Sackmann. 1998. Impedance spectroscopy of porin and gramicidin pores reconstituted into supported lipid bilayers on indium-tin-oxide electrodes. Langmuir 14(11):3118-3125.
4. Sugihara, K., J. Voros, and T. Zambelli. 2010. The resistance of polyelectrolyte multilayers in a free-hanging configuration. J Phys Chem B 114(44):13982-13987.
5. Tsemperouli, M., and K. Sugihara. 2018. Characterization of di-4-ANEPPS with nano-black lipid membranes. Nanoscale 10(3):1090-1098.
6. Hille, B. 1986. Ionic channels: molecular pores of excitable membranes. Harvey Lect 82:47-69.